

Beamforming and Waveform Optimization for RF Wireless Power Transfer with Beyond Diagonal Reconfigurable Intelligent Surfaces

Amirhossein Azarbahram, *Graduate Student Member, IEEE*, Onel L. A. López, *Senior Member, IEEE*, Bruno Clerckx, *Fellow, IEEE*, Marco Di Renzo, *Fellow, IEEE*, and Matti Latva-Aho, *Fellow, IEEE*

Abstract—Radio frequency (RF) wireless power transfer (WPT) is a promising technology to seamlessly charge low-power devices, but its low end-to-end power transfer efficiency remains a critical challenge. To address the latter, low-cost transmit/radiating architectures, e.g., based on reconfigurable intelligent surfaces (RISs), have shown great potential. Beyond diagonal (BD) RIS is a novel branch of RIS offering enhanced performance over traditional diagonal RIS (D-RIS) in wireless communications, but its potential gains in RF-WPT remain unexplored. Motivated by this, we analyze a BD-RIS-assisted single-antenna RF-WPT system to charge a single rectifier, and formulate a joint beamforming and multi-carrier waveform optimization problem aiming to maximize the harvested power. We propose two solutions relying on semi-definite programming for fully connected BD-RIS and an efficient low-complexity iterative method relying on successive convex approximation. Numerical results show that the proposed algorithms converge to a local optimum and that adding transmit sub-carriers or RIS elements improves the harvesting performance. We show that the transmit power budget impacts the relative power allocation among different sub-carriers depending on the rectifier's operating regime, while BD-RIS shapes the cascade channel differently for frequency-selective and flat scenarios. Finally, we verify by simulation that BD-RIS and D-RIS achieve the same performance under pure far-field line-of-sight conditions (in the absence of mutual coupling). Meanwhile, BD-RIS outperforms D-RIS as the non-line-of-sight components of the channel become dominant.

Index Terms—RF wireless power transfer, reconfigurable intelligent surfaces, waveform optimization, passive beamforming.

I. INTRODUCTION

FUTURE wireless communication systems must ensure seamless green connectivity among numerous low-power devices. For this, it is essential to mitigate electronic waste resulting from battery replacements and reduce disruptions caused by battery depletion [1]–[3]. Energy harvesting (EH) technologies are fundamental enablers for this by providing wireless charging capability and promoting sustainable Internet of Things [4], [5]. EH devices may harvest energy

from readily available or from dedicated sources. However, the former, a.k.a, ambient EH, may not be possible in all environments and/or may call for large device form factors [6], while the latter is supported by wireless power transfer (WPT) technologies such as inductive coupling, laser power beaming, magnetic resonance coupling, and radio frequency (RF) radiation. Hereinafter, we focus on RF-WPT, which can provide multi-user wireless charging capability over large distances while using the wireless communications infrastructure.

A. Preliminaries

A WPT system comprises three key building blocks: i) energy transmitter (ET); ii) wireless channel; and iii) energy receiver (ER). The charging signal is generated and amplified using a direct current (DC) power source at the ET. Then, it is upconverted to RF and transmitted over the wireless channel. The ER collects the signal and converts it to DC for EH. Each block includes some power consumption and loss sources, which bring new challenges to the system design. In fact, a key challenge of WPT systems is their inherently low end-to-end power transfer efficiency (PTE), which is given by

$$e = \underbrace{\frac{P_{rf}^t}{P_{dc}^t}}_{e_1} \times \underbrace{\frac{P_{rf}^r}{P_{rf}^t}}_{e_2} \times \underbrace{\frac{P_{dc}^r}{P_{rf}^r}}_{e_3} = \frac{P_{dc}^r}{P_{dc}^t}. \quad (1)$$

Herein, e_1 is impacted by the power consumption sources at the transmitter side, such as high-power amplifier (HPA), while the channel losses, i.e., shadowing and fading, can decrease e_2 . Note that the RF-to-DC conversion inefficiency at the receiver side influences e_3 . Thus, it is important to address these and provide novel solutions to maximize efficiency.

Waveform optimization is required to enhance efficiency at the ER. In fact, multitone waveforms can leverage the ER's non-linearity and enhance the performance in terms of DC harvested power [7], [8]. Also, energy beamforming (EB) techniques can compensate for wireless channel losses by pointing the transmit signal effectively toward the ERs' direction. The transmitter architecture determines the type of EB, which can be either active or passive. An active EB leverages active antenna elements connected to dedicated RF chains, while a passive EB utilizes low-cost nearly passive elements. For instance, a fully digital transmitter comprises active antenna elements, each with a dedicated RF chain, leading to high cost but offering the best beamforming gain. On the other hand, analog architectures relying, e.g., on phase shifters, can reduce

A. Azarbahram, O. López, and M. Latva-Aho are with Centre for Wireless Communications (CWC), University of Oulu, Finland, (e-mail: {amirhossein.azarbahram, onel.alcarazlopez, matti.latva-aho}@oulu.fi). B. Clerckx is with the Department of Electrical and Electronic Engineering, Imperial College London, SW7 2AZ London, U.K., (e-mail: b.clerckx@imperial.ac.uk). M. Di Renzo is with Université Paris-Saclay, CNRS, CentraleSupélec, Laboratoire des Signaux et Systèmes, 3 Rue Joliot-Curie, 91192 Gif-sur-Yvette, France. (marco.di-renzo@universite-paris-saclay.fr), and with King's College London, Centre for Telecommunications Research – Department of Engineering, WC2R 2LS London, U.K. (marco.di_renzo@kcl.ac.uk).

the cost but also degrade the performance. There exist hybrid architectures, which combine the two mentioned architectures, leading to a reduced number of RF chains and a tradeoff between cost/complexity and performance [9].

Traditional analog and hybrid architectures still need to cope with the challenges caused by complex analog networks. There are novel transmit architectures that avoid this additional complexity and provide EB gains at a much lower cost. For instance, dynamic metasurface antennas (DMA) utilize a limited number of RF chains, each one feeding multiple antenna elements on a waveguide [10], [11]. Moreover, reconfigurable intelligent surfaces (RIS) have become popular to enhance performance in wireless systems, especially in the presence of blockages/obstacles. This emerging technology may rely on planar surfaces comprising nearly passive scattering elements that introduce amplitude and phase changes to incident electromagnetic waves. Therefore, reflective-type RIS can smartly tune the reflected signal and point it toward the desired direction, providing significant EB gains [12]. In addition to reflective-type RIS, there exist some novel RIS-based architectures such as active RIS providing extra capabilities at the transmitter [13], or reflective-refractive models [14].

A recent generalization of diagonal RIS (D-RIS) is given by beyond diagonal RIS (BD-RIS), which is characterized by scattering matrices not constrained to be diagonal, thus elements/ports interconnected via tunable impedances [15]. The optimality of BD-RIS in lossless designs was proved in [16]. BD-RIS, through reconfigurable inter-connections, enables impinging waves to flow through the surfaces, hence a new degree of freedom and higher flexibility to manipulate waves by forming fully-, group-, tree-, and forest-connected structures [16], [17]. The former provides the highest flexibility in shaping the reflected signal, though lower complexities based on tree- and forest-connected architectures are attractive to achieve the performance-complexity Pareto frontier [17], [18]. Note that decreasing the number of connections between the scattering elements reduces both the performance gains and complexity, showcasing an interesting performance-complexity trade-off. BD-RIS is a general framework enabling multiple modes, such as reflective, hybrid, transmissive and reflective, and multi-sector, while encompassing other RIS architectures as special cases [19], [20].

B. Prior Works

Waveform and EB optimization for WPT with non-linear EH has received significant research attention, although most works focus on traditional fully digital transmitters. For instance, the authors of [21] propose transmit and receive EB solutions for a fully digital multiple-input multiple-output (MIMO) system to increase the DC harvested power, demonstrating the superiority of RF over DC combining. The authors of [22] investigate the design of WPT waveforms for different EH models and show that waveforms designed considering nonlinear EH yield substantial improvements in harvested DC power. Interestingly, in [23], the authors propose a low-complexity channel-adaptive waveform design for single-ER WPT systems leading to near-optimal EH performance. In [24], a low-complexity near-optimal EB is proposed for maximizing the weighted sum harvested DC power in multi-

ER scenarios. Moreover, the waveform and EB optimization problem for large-scale multi-antenna WPT systems has been investigated in [25], demonstrating the effectiveness of large-scale WPT deployments in improving the PTE. The authors of [26] leverage EB and optimized multi-sine waveforms in a MIMO WPT system and show that the joint optimization leads to significant gains compared to EB-only designs in terms of harvested power. All mentioned studies considered just the EH non-linearity, while [27] considers both HPA and rectifier's non-linearity. Therein, it is shown that the waveform design considering HPA non-linearity leads to significant gains compared to the ones focusing only on the rectifier. Moreover, multiple works, e.g., [28]–[30], focus on RF power maximization by considering linear EH for fully digital WPT.

Novel low-cost WPT transmit architectures for reducing the implementation cost/complexity is another topic gaining attention recently. The authors of [31] study the waveform and EB optimization for DMA-assisted WPT systems and show that DMA can be used to meet the DC requirement of the ERs with considerably fewer RF chains compared to a fully-digital counterpart. The authors of [32] propose a minimum-power beamforming design for simultaneous wireless information and power transfer (SWIPT) systems with a hybrid transmit architecture. The authors of [33] derive the number of RIS elements in an RIS-aided WPT system required to outperform traditional WPT relying on active antenna elements. Interestingly, the harvested power maximization problem is addressed in [34], [35] for RIS-aided WPT and SWIPT systems with non-linear EH, respectively. Therein, the authors highlight the extra beamforming gains on the harvested DC power provided by RISs, although only focusing on conventional D-RIS. Note that BD-RIS architectures have been widely investigated for communication purposes [15]–[17], [36], [37], while current research on RIS-aided WPT is still limited to conventional diagonal (local) RIS [34], [35]. Notably, another important yet unexplored topic is the use of BD-RIS for SWIPT systems with non-linear EH models. However, this work focuses on WPT alone, noting that maximizing the harvested DC power is first crucial as it directly impacts the achievable information transmission rate in SWIPT systems.

C. Contributions

Efficient WPT system design and optimization requires accurate non-linear EH models [8], [22]. However, most existing works employing non-linear EH primarily focus on traditional fully digital WPT designs. In contrast, this paper investigates BD-RIS-assisted WPT under non-linear EH models, a novel direction not yet explored.¹ Our main contributions are:

First, we formulate a joint EB and waveform optimization problem for a single-input single-output (SISO) multi-carrier BD-RIS-aided WPT system to maximize the DC harvested power. For this, we assume there is no direct path between the ET and ER. Our problem requires novel solutions because i) the methods available in the literature for D-RIS [34]

¹This work is an extension of our conference paper [38], wherein we present a BD-RIS EB and waveform optimization algorithm. In the current work, we propose two other solutions for BD-RIS beamforming and an efficient iterative solution for waveform optimization. Moreover, we provide thorough algorithm performance comparisons and a comprehensive waveform behavior analysis.

do not apply to BD-RIS due to the additional mathematical complexity caused by the non-diagonal scattering matrix; ii) our considered problem is different from existing ones in the BD-RIS literature, e.g., [17], [36], which focus on RF power maximization. The reason is that the DC harvested power depends on the fourth moment of the signal in addition to the second moment, a.k.a., RF power. Thus, the multi-carrier signal must be optimized such that the EH non-linearity is leveraged efficiently and the DC power is maximized [22].

Second, we decouple the waveform optimization and EB problem via alternating optimization, and propose:

- i) An efficient iterative method relying on successive convex approximation (SCA) and Karush–Kuhn–Tucker (KKT) conditions for the waveform optimization problem.
- ii) An EB optimization framework by relying on SCA and semi-definite programming (SDP), which models the rank-1 constraint using the atomic and Frobenius norms [39] and guarantees solution feasibility.
- iii) A semi-definite relaxation (SDR)-based EB method with lower time complexity compared to the one relying on SDP due to fewer approximations.
- iv) An efficient iterative EB method by leveraging the Neumann series approximation, SCA, and KKT conditions. Specifically, we approximate the problem using local convex subproblems, which can be solved using SCA. Then, we leverage the KKT conditions to solve each subproblem and an iterative method using low-complexity closed-form expressions to update the optimization variables. The computational complexity of the iterative method is reduced compared to the SDR-based approach from the fourth to the second degree of the number of RIS elements.

Third, we verify by simulations that:

- i) The proposed algorithms converge to a local optimum solution, while the convergence time scales with the number of sub-carriers and RIS elements.
- ii) The SDR-based algorithm achieves the optimal performance for a single-carrier system, while it outperforms the proposed iterative method in terms of harvested DC power for multi-carrier systems.
- iii) Increasing the number of sub-carriers or RIS elements improves the performance in terms of harvested DC power.
- iv) The frequency selectivity of the channel impacts the way that BD-RIS shapes the cascade channel, leading to performance changes. Specifically, when the channel tends to be frequency-flat, the BD-RIS can shape the cascade channel more effectively due to its frequency-flat nature. On the other hand, the variation among different sub-carriers of the cascade channel is higher for a frequency-selective case since BD-RIS impacts the channels at different sub-carriers differently.
- v) The transmit power budget impacts the relative power allocation of the designed waveform depending on the input RF power to the rectifier.
- vi) BD-RIS does not introduce any additional performance gains in terms of harvested DC power compared to D-RIS in far-field line-of-sight (LoS) channels (in the absence of mutual coupling) even with multi-carrier signals. On the other hand, in Rician channels with non-LoS (NLoS) components, BD-RIS outperforms D-RIS by effectively tuning the cascade channel,

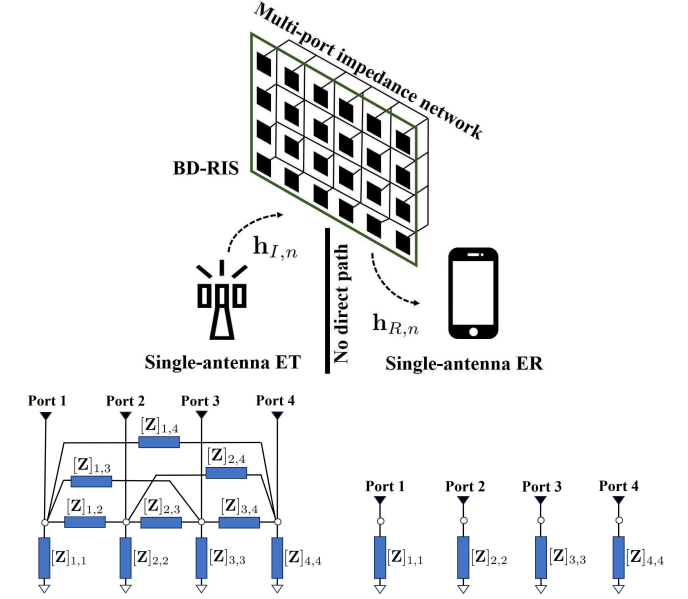


Fig. 1: Illustration of (a) the system model comprising a single-antenna ET, a BD-RIS, and a single-antenna ER; and (b) examples of 4-port impedance networks for fully-connected BD-RIS (bottom-left) and D-RIS (bottom-right).

leading to increased harvested DC power. This extends the findings of [16] to multi-carrier WPT.

The remainder of the paper is structured as follows. Section II introduces the system model and problem formulation. The optimization framework for beamforming and waveform design is elaborated in Section III. Section IV presents the numerical results, while Section V concludes the paper.

Notations: Bold lower-case and upper-case letters represent vectors and matrices. The ℓ_2 -norm operator is denoted by $\|\cdot\|$, while $\|\cdot\|_*$ and $\|\cdot\|_F$ are the atomic and Frobenius norm, respectively. $\Re\{\cdot\}$ and $\Im\{\cdot\}$ denote the real and imaginary parts of a complex matrix or scalar. Moreover, $(\cdot)^T$, $(\cdot)^H$, and $(\cdot)^*$ denote the transpose, transposed conjugate, and conjugate, respectively. Additionally, $[\cdot]_{i,l}$ denotes the element in the l th column and the i th row of a matrix. The vectorization operator is represented by $\text{Vec}(\cdot)$, and its inverse is denoted by $\text{Vec}_{D \times D}^{-1}(\cdot)$. Finally, \mathbf{I}_D represents a $D \times D$ identity matrix and $\text{diag}(\mathbf{a})$ is a diagonal matrix with its main diagonal being the elements of vector \mathbf{a} .

II. SYSTEM MODEL & PROBLEM FORMULATION

We consider a SISO WPT system with N sub-carriers aided by a BD-RIS consisting of M elements. The adoption of multitone waveforms is motivated by their ability to exploit the rectifier's non-linearity to improve the performance [8]. For simplicity, we assume perfect channel state information at the ET as in [15], [22], [34]. Moreover, we assume there is no direct path between the ET and the ER, which is motivated by typical RIS applications to improve coverage in areas with blockages. The system model and the path of the incident and reflecting channels at the n th sub-carrier are illustrated in Fig. 1.a. This section describes the transmit and receive signals, BD-RIS, rectenna, and the problem formulation.

A. Transmit/Receive Signals and BD-RIS

We consider N sub-carriers with $f_n = f_c + (n-1)\Delta f$ being the frequency of the n th sub-carrier, where f_c is the lowest frequency and Δf is the sub-carrier spacing. Thus, the transmit signal at time t can be written as $\Re\{\sum_{n=1}^N s_n e^{j2\pi f_n t}\}$, where s_n is the complex weight of the n th sub-carrier.² The transmit signal propagates through the wireless channel. We denote by $\mathbf{h}_{I,n} \in \mathbb{C}^{M \times 1}$ the channel between the transmitter and RIS and by $\mathbf{h}_{R,n} \in \mathbb{C}^{M \times 1}$ the channel between the RIS and receiver for the n th sub-carrier.

Assuming a multiport network model, each D-RIS element is modeled as a port connected to an independent tunable impedance [16], [40], [41]. This leads to the so-called D-RIS model, which is mathematically characterized by diagonal phase-shift matrices. In BD-RIS, the matrix of tunable elements $\mathbf{Z} \in \mathbb{C}^{M \times M}$ has non-zero off-diagonal entries [17]. Thus, the scattering matrix can be formulated as [40]

$$\Theta = (\mathbf{Z} + Z_0 \mathbf{I}_M)^{-1}(\mathbf{Z} - Z_0 \mathbf{I}_M), \quad (2)$$

where Z_0 denotes the reference impedance. In the case of reciprocal and lossless BD-RIS,³ the scattering matrix is symmetric ($\Theta = \Theta^T$) and unitary ($\Theta^H \Theta = \mathbf{I}_M$). Note that in the case of fully-connected BD-RIS, all the elements in \mathbf{Z} can be non-zero, while for other sub-architectures, some off-diagonal entries become zero, and for D-RIS, \mathbf{Z} becomes diagonal. Fig. 1.b illustrates an example of a 4-port impedance network for fully-connected BD-RIS and D-RIS.

The cascade channel at the n th sub-carrier is written as $h_n = \mathbf{h}_{R,n}^T \Theta \mathbf{h}_{I,n}$,⁴ and the received signal at time t is given by $y(t) = \sum_{n=1}^N \Re\{s_n h_n e^{j2\pi f_n t}\}$.

B. Rectenna

The ER model, i.e., rectenna, consists of the antenna equivalent circuit and a single-diode rectifier for transforming the RF received signal into DC [8], [22], [31]. By leveraging this model, assuming perfect matching, and using the Taylor's expansion, the output current of the rectenna is given by

$$i_{dc} = \sum_{i \text{ even}, i \geq 2}^{\bar{n}} K_i \mathbb{E}\{y(t)^i\}, \quad (3)$$

where K_2, K_4 are determined by the characteristics of the rectifier circuit. One can consider $\bar{n} = 4$ and model the main sources of non-linearity using the fourth order term, while the second order term represents the ideal linear rectenna model [22], [34]. Note that (3) requires averaging over time samples, which makes the optimization extremely challenging due to the need to consider a high sampling rate for achieving suffi-

cient accuracy. Fortunately, by expressing (3) in the frequency domain and assuming $n_0 = 4$, we obtain [22]

$$i_{dc} = \frac{K_2}{2} \sum_n \|s_n h_n\|^2 + \frac{3K_4}{8} \sum_{\substack{n_0, n_1, n_2, n_3 \\ n_0 + n_1 = n_2 + n_3}} (h_{n_0} s_{n_0})^* \dots (h_{n_1} s_{n_1})^* (h_{n_2} s_{n_2}) (h_{n_3} s_{n_3}), \quad (4)$$

which is more tractable than the sampling-dependent model.

C. Problem Formulation

We aim to maximize the harvested power given a transmit power budget, P_T . By leveraging the fact that the DC harvested power is an increasing function of the DC current at the ER, the problem can be formulated as

$$\underset{s_n, \Theta}{\text{maximize}} \quad i_{dc} \quad (5a)$$

$$\text{subject to} \quad \Theta = \Theta^T, \quad (5b)$$

$$\Theta^H \Theta = \mathbf{I}_M, \quad (5c)$$

$$\frac{1}{2} \sum_{n=1}^N \|s_n\|^2 \leq P_T. \quad (5d)$$

Notably, (5) is a non-convex problem due to the unitary constraint, the i_{dc} non-linearity, and the coupling between the variables. To cope with this, we decouple (5) into separate problems for optimizing waveform and beamforming and leverage alternating optimization to solve it.

III. BEAMFORMING AND WAVEFORM OPTIMIZATION

Here, we provide optimization methods for solving the beamforming and waveform-related subproblems. First, we propose a low-complexity iterative method for waveform optimization problems relying on SCA and KKT conditions. Then, we leverage SDP, SDR, SCA, and KKT conditions to solve the beamforming subproblem using different approaches.

A. Waveform Optimization with Fixed h_n

First, we assume the cascade channel h_n to be fixed and optimize the signal weights $s_n, \forall n$. We proceed by defining $s_n = \bar{s}_n e^{j\tilde{s}_n}$, where \bar{s}_n and \tilde{s}_n are the amplitude and the phase of s_n , respectively. Similarly, we can write $h_n = \bar{h}_n e^{j\tilde{h}_n}$. It is evident that the optimal \tilde{s}_n must compensate for the phases in (4), leading to a real-valued i_{dc} [7]. Thus, it is sufficient to have $\tilde{s}_n^* = -\tilde{h}_n, \forall n$ leading to $\bar{s}_n e^{j\tilde{s}_n^*} h_n = \bar{s}_n \bar{h}_n, \forall n$. Now the only goal of the optimization is to find the optimal amplitudes for the signal weights at different sub-carriers. For this, the problem for a given Θ can be reformulated as

$$\underset{\bar{s}_n}{\text{maximize}} \quad i_{dc} \quad (6a)$$

$$\text{subject to} \quad \frac{1}{2} \sum_{n=1}^N \bar{s}_n^2 \leq P_T. \quad (6b)$$

Lemma 1. The DC current i_{dc} in (4) is convex w.r.t. \bar{s}_n .

Proof. Note that $y(t)$ is linear w.r.t. \bar{s}_n . By leveraging the second-order convexity condition [42] and the linearity of the mathematical average operator, it can be easily verified that i_{dc}

²We assume a linear model for the HPA being mainly interested in the impact of non-linear rectennas. Notably, this is a valid assumption for a proper transmit power such that the HPA does not enter the saturation region [27].

³For simplicity and since the goal is to investigate the gains of BD-RIS for WPT, we consider the case with no mutual coupling between different ports.

⁴The underlying general model and assumptions can be seen in [41].

is convex w.r.t. $y(t)$. Then, i_{dc} is convex w.r.t. \bar{s}_n since the composition of an affine with a convex function is convex. \square

According to Lemma 1, problem (6) is not convex since it deals with the maximization of a convex function. However, the convexity of (6a) leads to the fact that $\tilde{i}_{dc}(\bar{s}_n, \bar{s}_n^{(l)}) \leq i_{dc}$, where $\tilde{i}_{dc}(\bar{s}_n, \bar{s}_n^{(l)})$ is the first order Taylor's expansion of i_{dc} at the local point $\bar{s}_n^{(l)}$, formulated as

$$\tilde{i}_{dc}(\bar{s}_n, \bar{s}_n^{(l)}) = i_{dc}|_{\bar{s}_n = \bar{s}_n^{(l)}} + \sum_{n=1}^N g(\bar{s}_n^{(l)})(\bar{s}_n - \bar{s}_n^{(l)}), \quad (7)$$

where

$$g(\bar{s}_n) = K_2 \bar{h}_n^2 \bar{s}_n + \frac{3K_4}{2} \left[\bar{h}_n^4 \bar{s}_n^3 + 2 \sum_{n_1 \neq n} \bar{h}_n^2 \bar{h}_{n_1}^2 \bar{s}_{n_1}^2 \bar{s}_n + \sum_{\substack{n_2, n_3 \\ n_2 + n_3 = 2n \\ n_2 \neq n_3}} \bar{h}_{n_2} \bar{h}_{n_3} \bar{h}_n^2 \bar{s}_{n_2} \bar{s}_{n_3} \bar{s}_n + \sum_{\substack{n_1, n_2, n_3 \\ -n_1 + n_2 + n_3 = n \\ n \neq n_1 \neq n_2 \neq n_3}} \bar{h}_{n_1} \bar{h}_{n_2} \bar{h}_{n_3} \bar{s}_{n_1} \bar{s}_{n_2} \bar{s}_{n_3} \bar{h}_n \right]. \quad (8)$$

Hereby and by removing the constant terms (since they do not impact the optimization procedure), the problem can be transformed into a convex problem at the neighborhood of the initial point $\bar{s}_n^{(l)}$ as

$$\underset{\bar{s}_n}{\text{minimize}} \quad \xi_1 = - \sum_{n=1}^N g(\bar{s}_n^{(l)}) \bar{s}_n \quad (9a)$$

$$\text{subject to} \quad \frac{1}{2} \sum_{n=1}^N \bar{s}_n^2 \leq P_T. \quad (9b)$$

Finally, the problem can be iteratively solved using standard convex optimization tools, e.g., CVX [43].

However, utilizing standard solvers for the optimization problem in (9) requires solving a quadratic program [42] in each SCA iteration. Notably, the complexity of quadratic programs scales with a polynomial function of the problem size, while the degree of the polynomial mainly depends on the type of solver. Let us consider a simple solver based on the Newton method, which has $\mathcal{O}(n^3)$ complexity [42], where n is the problem size, leading to n scaling with the number of variables N . Therefore, solving problems such as (9) using standard tools is not computationally efficient.

Theorem 1. *The local solution of (9) can be updated using*

$$\bar{s}_n^{(l+1)} = \bar{s}_n^{(l)} + \rho_s (\bar{s}_n^* - \bar{s}_n^{(l)}), \quad (10)$$

where $\rho_s \leq 1$ is a convergence control parameter,

$$\bar{s}_n^* = \frac{g(\bar{s}_n^{(l)})}{\lambda^{(l)}}, \quad \forall n, \quad (11)$$

$$\lambda^{(l)} = \sqrt{\frac{1}{2P_T} \sum_{n=1}^N g(\bar{s}_n^{(l)})^2}. \quad (12)$$

Proof. The proof is provided in Appendix A.

Algorithm 1 Iterative waveform optimization (IT-WF).

- 1: **Input:** $\{h_n\}_{\forall n}$, ρ_s , v **Output:** $\bar{s}_n^{(l)}$
 - 2: **Initialize:** Initialize $\bar{s}_n^{(l)}$, $\forall n$ using (13), $\xi_1 = \infty$
 - 3: **repeat**
 - 4: $\xi_1^* \leftarrow \xi_1$, compute $\lambda^{(l)}$ using (12)
 - 5: Obtain $\bar{s}_n^{(l+1)}$, $\forall n$ using (11) and (10)
 - 6: $\bar{s}_n^{(l+1)} \leftarrow \bar{s}_n^{(l+1)} e^{-j\tilde{h}_n}$, $\forall n$
 - 7: Compute ξ_1 using (9a), $\bar{s}_n^{(l)} \leftarrow \bar{s}_n^{(l+1)}$, $l \leftarrow l + 1$
 - 8: **until** $\|1 - \xi_1^*/\xi_1\| \leq v$
-

Leveraging Theorem 1 to iteratively solve (9) leads to considerably lower computation complexity since closed-form expressions are utilized in each SCA iteration. Algorithm 1 illustrates the proposed iterative method for obtaining \bar{s}_n , $\forall n$. First, the scaled matched filter approach, proposed in [23], is used to initialize the signal weights such that

$$s_n = e^{-j\tilde{h}_n} \bar{h}_n^\beta \sqrt{\frac{2P_T}{\sum_{n_0=1}^N \bar{h}_{n_0}^{2\beta}}}, \quad \forall n. \quad (13)$$

Then, the optimization variables and the corresponding dual variable are updated iteratively until convergence. By leveraging the lower-bound properties of Taylor's approximation and writing the KKT conditions of (6), it can be seen that (9a) is monotonically increasing and the obtained solution by Algorithm 1 satisfies the KKT conditions of (6).

B. SDR-based Beamforming for Fully Connected BD-RIS

Herein, we provide an optimization method for the beamforming problem given s_n , $\forall n$. Note that this approach only applies to fully connected BD-RIS since it directly deals with Θ as the optimization variable. Let us proceed by rewriting (5) for fixed s_n as

$$\underset{\Theta}{\text{maximize}} \quad i_{dc} \quad (14a)$$

$$\text{subject to} \quad (5b), (5c),$$

which is highly complicated and non-convex due to the unitary constraint and the i_{dc} non-linearity.

Proposition 1. *The cascade channel, i.e., $h_n = \mathbf{h}_{R,n}^T \Theta \mathbf{h}_{I,n}$, can be rewritten as*

$$h_n = \mathbf{a}_n^T \boldsymbol{\theta}, \quad (15)$$

where $\mathbf{a}_n = \mathbf{P}^T \text{Vec}(\mathbf{h}_{I,n} \mathbf{h}_{R,n}^T) \in \mathbb{C}^{M(M+1)/2 \times 1}$. Moreover, $\boldsymbol{\theta} \in \mathbb{C}^{M(M+1)/2 \times 1}$ is the vector containing the lower/upper-triangle elements in Θ and $\mathbf{P} \in \{0, 1\}^{M^2 \times M(M+1)/2}$ is a permutation matrix such that

$$[\mathbf{P}]_{M(m-1)+n, k} = \begin{cases} 1, & k = m(m-1)/2 + n, \quad 1 \leq n \leq m \\ 1, & k = n(n-1)/2 + m, \quad m < n \leq M \\ 0, & \text{otherwise.} \end{cases} \quad (16)$$

Proof. The proof is provided in Appendix B

Leveraging Proposition 1 allows us to remove the constraint (5b) by using $\boldsymbol{\theta}$ as the optimization variable. However, the complexity caused by the unitary constraint still remains. For this, we leverage the idea in [34] and define $\mathbf{z}_n = s_n \mathbf{a}_n$,

$\mathbf{D}_0 = \mathbf{z}_1 \mathbf{z}_1^H + \dots + \mathbf{z}_N \mathbf{z}_N^H$, $\mathbf{D}_1 = \mathbf{z}_1 \mathbf{z}_2^H + \dots + \mathbf{z}_{N-1} \mathbf{z}_N^H$, and $\mathbf{D}_{N-1} = \mathbf{z}_1 \mathbf{z}_N^H$. Hereby, i_{dc} can be reformulated as

$$i_{dc} = \frac{1}{2} K_2 \boldsymbol{\theta}^H \mathbf{D}_0 \boldsymbol{\theta} + \frac{3}{8} K_4 \boldsymbol{\theta}^H \mathbf{D}_0 \boldsymbol{\theta} (\boldsymbol{\theta}^H \mathbf{D}_0 \boldsymbol{\theta})^H + \frac{3}{4} K_4 \sum_{n=1}^{N-1} \boldsymbol{\theta}^H \mathbf{D}_n \boldsymbol{\theta} (\boldsymbol{\theta}^H \mathbf{D}_n \boldsymbol{\theta})^H. \quad (17)$$

Next, we need to formulate the constraint (5c) as a function of the new optimization variable $\boldsymbol{\theta}$. For this, let us proceed by defining a permutation matrix \mathbf{P}_i , which extracts the i th row of $\boldsymbol{\Theta}$ from $\boldsymbol{\theta}$. Hereby, (5c) can be rewritten as

$$(\mathbf{P}_i \boldsymbol{\theta})^H (\mathbf{P}_j \boldsymbol{\theta}) = \text{Tr}(\boldsymbol{\theta} \boldsymbol{\theta}^H \bar{\mathbf{P}}_{i,j}) = \begin{cases} 1, & i = j, \\ 0, & i \neq j, \end{cases} \quad (18)$$

where $\bar{\mathbf{P}}_{i,j} = \mathbf{P}_i^T \mathbf{P}_j$ and \mathbf{P}_i is a permutation matrix containing the $(iM - M + 1)$ th to the iM th row of \mathbf{P} .

Now, we define $d_n = \boldsymbol{\theta}^H \mathbf{D}_n \boldsymbol{\theta}$, $\mathbf{d} = [d_1, \dots, d_N]^T$, and positive semidefinite matrices $\mathbf{K}_0 = \text{diag}\{\frac{3}{8}K_4, \frac{3}{4}K_4, \dots, \frac{3}{4}K_4\} \succeq 0$ and $\mathbf{X} = \boldsymbol{\theta} \boldsymbol{\theta}^H$. Hereby, the problem can be reformulated as

$$\underset{\mathbf{d}, \mathbf{X} \succeq 0}{\text{maximize}} \quad \frac{1}{2} K_2 d_0 + \mathbf{d}^H \mathbf{K}_0 \mathbf{d} \quad (19a)$$

$$\text{subject to} \quad \text{Tr}(\mathbf{X} \bar{\mathbf{P}}_{i,j}) = 1, \quad \forall i = j, \quad (19b)$$

$$\text{Tr}(\mathbf{X} \bar{\mathbf{P}}_{i,j}) = 0, \quad \forall i \neq j, \quad (19c)$$

$$d_n = \text{Tr}(\mathbf{X} \mathbf{D}_n), \quad \forall n, \quad (19d)$$

$$\text{rank}(\mathbf{X}) = 1. \quad (19e)$$

Note that problem (19) is still non-convex and challenging to solve since it deals with the maximization of a convex objective function and includes a rank-1 constraint. For (19a), SCA can be used to iteratively update the objective function by approximating it using its first-order Taylor's expansion. Specifically, the quadratic term in (19a) can be approximated in the neighborhood of $\mathbf{d}^{(l)}$ by [34]

$$f(\mathbf{d}, \mathbf{d}^{(l)}) = 2\Re\{\mathbf{d}^{(l)H} \mathbf{K}_0 \mathbf{d}\} - \mathbf{d}^{(l)H} \mathbf{K}_0 \mathbf{d}^{(l)}. \quad (20)$$

Since $f(\mathbf{d}, \mathbf{d}^{(l)}) \leq \mathbf{d}^H \mathbf{K}_0 \mathbf{d}$ always holds, it can be used as a lower bound and maximizing the Taylor's approximation iteratively leads to maximizing the original quadratic term. Note that (19e) can be equivalently written as

$$\|\mathbf{X}\|_* - \|\mathbf{X}\|_F \leq 0, \quad (21)$$

which is non-convex since it deals with the difference of two convex functions. However, the right-hand-side term can be approximated using its first-order Taylor's expansion at a local point $\bar{\mathbf{X}}$. Specifically, $\|\mathbf{X}\|_F$ can be replaced by a convex lower-bound given by [39]

$$f(\mathbf{X}, \bar{\mathbf{X}}) = \|\bar{\mathbf{X}}\|_F + \Re\left\{\sum_{i,l} \frac{[\bar{\mathbf{X}}]_{i,l}}{\|\bar{\mathbf{X}}\|_F} ([\mathbf{X}]_{i,l} - [\bar{\mathbf{X}}]_{i,l})^*\right\}. \quad (22)$$

Hereby, (19) can be reformulated as

$$\underset{\mathbf{X}}{\text{minimize}} \quad \Omega = \text{Tr}(\mathbf{K}_1 \mathbf{X}) \quad (23a)$$

$$\text{subject to} \quad \|\mathbf{X}\|_* - f(\mathbf{X}, \bar{\mathbf{X}}) \leq 0, \quad (23b)$$

$$\mathbf{X} \succeq 0, \quad (23c)$$

$$(19b), (19c),$$

where $\mathbf{K}_1 = \mathbf{J} + \mathbf{J}^H$ and

$$\mathbf{J} = -\frac{K_2}{4} \mathbf{D}_0 - \frac{3K_4}{8} d_0^{(l)} \mathbf{D}_0 - \frac{3K_4}{4} \sum_{n=1}^{N-1} d_n^{(l)} \mathbf{D}_n. \quad (24)$$

This problem is a standard SDP that can be solved using convex optimization tools such as CVX [43]. Note that iteratively solving (23) leads to convergence to a rank-1 solution, which is a local optimum solution of (19).⁵ However, this approach requires many iterations for convergence since \mathbf{X} is a large matrix and the approximation is done in both the objective function and a constraint. To cope with this complexity, we use SDR to reformulate the problem in the neighborhood of the initial point $\mathbf{d}^{(l)}$ as

$$\underset{\mathbf{X}}{\text{minimize}} \quad \Omega = \text{Tr}(\mathbf{K}_1 \mathbf{X}) \quad (25a)$$

$$\text{subject to} \quad (19b), (19c), (23c),$$

which is also a standard SDP similar to (23). Moreover, if the obtained \mathbf{X}^* is a rank-1 matrix, the SDR is tight and \mathbf{X}^* is a stationary point of problem (25), leading to a local optimum point extracted by $\mathbf{X}^* = \boldsymbol{\theta}^* \boldsymbol{\theta}^{*H}$. Then, $\boldsymbol{\theta}^*$ can be used to obtain $\boldsymbol{\Theta}^* = \text{Vec}^{-1}(\mathbf{P} \boldsymbol{\theta}^*)$. However, it might happen that $\text{rank}(\mathbf{X}^*) > 1$, which is the case that \mathbf{X}^* satisfies the KKT conditions of problem (25) (see [34] for the proof). For this, we obtain an approximate $\boldsymbol{\theta}^*$ using the Gaussian randomization method in [44]. Note that in this case, using $\boldsymbol{\theta}^*$ to construct $\boldsymbol{\Theta}$ leads to a symmetric $\boldsymbol{\Theta}$, but not necessarily a unitary matrix. Thus, it is essential to map the final solution into the feasible space of the problem. Let us proceed by writing $\boldsymbol{\Theta}' = \text{Vec}^{-1}(\mathbf{P} \boldsymbol{\theta}^*)$. Then, by leveraging the fact that $\boldsymbol{\Theta}'$ is symmetric, we can write the singular value decomposition (SVD) as $\boldsymbol{\Theta}' = \mathbf{Q} \boldsymbol{\Sigma} \mathbf{Q}^T$, where \mathbf{Q} is a unitary matrix and $\boldsymbol{\Sigma}$ is a diagonal matrix containing the singular values of $\boldsymbol{\Theta}'$. It is evident that if the diagonal elements of $\boldsymbol{\Sigma}$ are unit modulus, $\boldsymbol{\Theta}'$ is unitary. However, this is only the case when $\text{rank}(\mathbf{X}^*) = 1$ and SDR is tight, while for higher-rank cases, we propose a randomization-based method to obtain a feasible solution.

Algorithm 2 describes the proposed SDR-based method for beamforming and waveform optimization for fully connected BD-RIS. First, the optimization variables are initialized. Then, the waveform and scattering matrix are optimized in an alternative fashion through lines 7-17. Specifically, beamforming is done by solving (25) iteratively in lines 9-14, followed by iterative waveform optimization using Algorithm 1. Finally, Algorithm 3 is utilized to construct a feasible solution $\boldsymbol{\Theta}^*$ based on the characteristics of the obtained solution $\boldsymbol{\Theta}$. First, the SVD of $\boldsymbol{\Theta}$ is computed to obtain a unitary matrix \mathbf{Q} . Then, random phase shifts are generated for K iterations to construct new $\boldsymbol{\Sigma}'$ matrices and their corresponding feasible solution $\boldsymbol{\Theta}$. Finally, the constructed $\boldsymbol{\Theta}$ with the best i_{dc} is selected.

C. Iterative Beamforming Optimization

Herein, we provide an alternative low-complexity optimization method for the beamforming problem, which applies to any BD-RIS structure since it deals with the \mathbf{Z} matrix as the optimization variable. Let us proceed by defining \mathcal{G}_Z as the set

⁵The proof is similar to the one provided in [34].

Algorithm 2 SDR-based beamforming and waveform optimization for fully connected BD-RIS (SDR-BDRIS).

```

1: Input:  $v, \beta, \mathbf{h}_{R,n}, \mathbf{h}_{I,n}, \forall n$    Output:  $s_n^{(l)}, \forall n, \Theta^*$ 
2: Initialize:
3:  $f^* = 0, i_{dc} = \infty, [\mathbf{Z}_{i,m}] = j\mathbf{Z}_0, \forall i, m,$ 
4:  $\Theta^{(l)} = (\mathbf{Z} + Z_0\mathbf{I}_M)^{-1}(\mathbf{Z} - Z_0\mathbf{I}_M)$ 
5: Compute  $\mathbf{P}, h_n,$  and  $s_n^{(l)}$  using (16), (15), and (13)
6: Compute  $d_n^{(l)} = \theta^{(l)}\mathbf{D}_n\theta^{(l)H}$ , where  $\theta^{(l)} = \mathbf{P}^{-1}\text{Vec}(\Theta^{(l)})$ 
7: repeat
8:    $\Omega = \infty, i_{dc}^* \leftarrow i_{dc}$ 
9:   repeat
10:     $\Omega^* \leftarrow \Omega$ , solve (25) to obtain  $\mathbf{X}$ 
11:    Compute  $\theta^{(l)}$  using Gaussian randomization
12:     $d_n^{(l)} = \theta^{(l)}\mathbf{D}_n\theta^{(l)H}$ ,  $\Theta^{(l)} = \text{Vec}^{-1}(\mathbf{P}\theta^{(l)})$ 
13:     $l \leftarrow l + 1$ 
14:  until  $\|1 - \Omega^*/\Omega\| \leq v$ 
15:   $h_n = \mathbf{h}_{R,n}^T \Theta^{(l)} \mathbf{h}_{I,n}$  and run Algorithm 1 to update  $s_n^{(l)}$ 
16:  Compute  $i_{dc}$  using (4)
17: until  $\|1 - i_{dc}^*/i_{dc}\| \leq v$ 
18: Run Algorithm 3 to obtain  $\Theta^*$ 

```

Algorithm 3 Randomization-based method for obtaining a feasible Θ .

```

1: Input:  $\Theta, K, \mathbf{h}_{R,n}, \mathbf{h}_{I,n}, s_n, \forall n$    Output:  $\Theta^*$ 
2: Initialize: Compute SVD of  $\Theta$  as  $\Theta = \mathbf{Q}\Sigma\mathbf{Q}^T, i_{dc}^* = 0$ 
3: for  $k = 1, \dots, K$  do
4:   Generate random  $\phi_i \in [0, 2\pi], \forall i$ 
5:   Set  $\phi = [e^{j\phi_1}, \dots, e^{j\phi_M}]^T$  and  $\Sigma' = \text{diag}(\phi)$ 
6:   Compute  $\Theta = \mathbf{Q}\Sigma'\mathbf{Q}^T$  and  $i_{dc}$  using (4)
7:   if  $i_{dc} > i_{dc}^*$ , then  $i_{dc}^* \leftarrow i_{dc}, \Theta^* \leftarrow \Theta$ 
8: end for

```

of possible impedance matrices, which relies on the BD-RIS structure and inter-connections. Then, we rewrite (14) as

$$\underset{\mathbf{Z}}{\text{maximize}} \quad i_{dc} \quad (26a)$$

$$\text{subject to} \quad \mathbf{Z} = \mathbf{Z}^T, \quad (26b)$$

$$\mathbf{Z} \in \mathcal{G}_{\mathcal{Z}}, \quad (26c)$$

which is a highly non-linear non-convex problem due to the matrix inverse term in (2). Thus, the first challenge is to deal with this term, which appears in h_n .

Proposition 2. By leveraging the Neumann approximation and defining Ω as a small increment to the impedance matrix \mathbf{Z} , such that $\|[\Omega]_{i,m}\| \leq \delta, \forall i, m$, we can write

$$(\mathbf{Z} + Z_0\mathbf{I}_M + \Omega)^{-1} \approx (\mathbf{Z} + Z_0\mathbf{I}_M)^{-1} - (\mathbf{Z} + Z_0\mathbf{I}_M)^{-1}\Omega(\mathbf{Z} + Z_0\mathbf{I}_M)^{-1}, \quad (27)$$

where δ must satisfy

$$\delta \ll \frac{1}{\|(\mathbf{Z}^{(l)} + Z_0\mathbf{I}_M)^{-1}\|_{\infty}}. \quad (28)$$

Proof. The proof is provided in Appendix C.

By leveraging Proposition 2, one can linearize h_n using the Neumann approximation and iteratively improve the approximation. Thus, by defining an auxiliary variable Ω as the increment to the impedance matrix $\mathbf{Z}^{(l)}$ at the l th iteration of the Neumann approximation, we can write

$$\begin{aligned} h_n^{(l)} &\approx \mathbf{h}_{R,n}^T (\mathbf{Z}^{(l)} + Z_0\mathbf{I}_M + \Omega)^{-1} (\mathbf{Z}^{(l)} - Z_0\mathbf{I}_M) \mathbf{h}_{I,n} \\ &\approx \mathbf{h}_{R,n}^T \left[(\mathbf{Z} + Z_0\mathbf{I}_M)^{-1} - (\mathbf{Z} + Z_0\mathbf{I}_M)^{-1}\Omega(\mathbf{Z} + Z_0\mathbf{I}_M)^{-1} \right] (\mathbf{Z}^{(l)} - Z_0\mathbf{I}_M) \mathbf{h}_{I,n} \\ &= \mathbf{h}_{R,n}^T \mathbf{A}^{(l)} (\mathbf{I}_M - \Omega \mathbf{A}^{(l)}) \mathbf{B}^{(l)} \mathbf{h}_{I,n} \\ &= \mathbf{a}_n^{(l)T} (\mathbf{I}_M - \Omega \mathbf{A}^{(l)}) \mathbf{b}_n^{(l)}, \quad \forall n, \end{aligned} \quad (29)$$

where $\mathbf{A}^{(l)} = (\mathbf{Z}^{(l)} + Z_0\mathbf{I}_M)^{-1}$, $\mathbf{a}_n^{(l)} = (\mathbf{h}_n^T \mathbf{A}^{(l)})^T$, $\mathbf{b}_n^{(l)} = \mathbf{B}^{(l)} \mathbf{h}_{I,n}$, and $\mathbf{B}^{(l)} = \mathbf{Z}^{(l)} - Z_0\mathbf{I}_M$.

By leveraging the linearization in (29), it can be easily verified that the objective in (26) can be approximated using Taylor's expansion. This allows for the problem to be solved using convex optimization tools, similar to the previous optimization case. As mentioned earlier, one needs to solve a quadratic program at each iteration for that purpose. This leads to the problem size scaling with the symmetric matrix subspace with size M^2 , making it computationally inefficient for large problems. To cope with this, we proceed by proposing an efficient iterative method to solve (26).

Proposition 3. Expression (29) can be rewritten as

$$h_n = \mathbf{a}_n^{(l)T} \mathbf{b}_n^{(l)} - \mathbf{f}_n^{(l)T} \boldsymbol{\omega}, \quad (30)$$

where $\mathbf{f}_n^{(l)} = \mathbf{P}^T \text{Vec}(\mathbf{A}^{(l)} \mathbf{b}_n^{(l)} \mathbf{a}_n^{(l)T}) \in \mathbb{C}^{M(M+1)/2 \times 1}$. Moreover, $\boldsymbol{\omega} \in \mathbb{C}^{M(M+1)/2 \times 1}$ is the vector containing the lower/upper-triangle elements in Ω and $\mathbf{P} \in \{0, 1\}^{M^2 \times M(M+1)/2}$ is the permutation matrix defined in (16).

Proof. By leveraging the same matrix properties provided in Appendix B, we proceed by rewriting

$$\begin{aligned} h_n &\approx \mathbf{a}_n^{(l)T} (\mathbf{I}_M - \Omega \mathbf{A}^{(l)}) \mathbf{b}_n^{(l)} \\ &= \mathbf{a}_n^{(l)T} \mathbf{b}_n^{(l)} - \text{Tr}(\Omega \mathbf{A}^{(l)} \mathbf{b}_n^{(l)} \mathbf{a}_n^{(l)T}) \\ &= \mathbf{a}_n^{(l)T} \mathbf{b}_n^{(l)} - \text{Vec}(\mathbf{A}^{(l)} \mathbf{b}_n^{(l)} \mathbf{a}_n^{(l)T})^T \text{Vec}(\Omega) \\ &= \mathbf{a}_n^{(l)T} \mathbf{b}_n^{(l)} - \text{Vec}(\mathbf{A}^{(l)} \mathbf{b}_n^{(l)} \mathbf{a}_n^{(l)T})^T \mathbf{P} \boldsymbol{\omega}, \end{aligned} \quad (31)$$

matching (30). \square

Lemma 2. The i_{dc} in (4) is convex w.r.t. $\boldsymbol{\omega}$.

Proof. It is evident from equation (30) that h_n is affine w.r.t. $\boldsymbol{\omega}$. Furthermore, i_{dc} is convex w.r.t. h_n , which can be easily proven using Lemma 1. Thus, i_{dc} w.r.t. $\boldsymbol{\omega}$ is a composition of an affine function and a convex function, which is convex. \square

Proposition 3 and Lemma 2 ensure that substituting (30) into (26a) leads to maximizing a convex objective function w.r.t. $\boldsymbol{\omega}$, which can be approximated similar to the waveform optimization procedure for fixed h_n . Specifically, the convex objective can be approximated using its first-order Taylor's

expansion at each local point and iteratively optimized. Thus, we proceed by writing the first-order Taylor's coefficient as

$$\begin{aligned} \mathbf{u}(\boldsymbol{\omega}) = & -K_2 \sum_n h_n \|s_n\|^2 \mathbf{f}_n^{(l)} + \\ & - \frac{3K_4}{8} \sum_{\substack{n_0, n_1, n_2, n_3 \\ n_0 + n_1 = n_2 + n_3}} s_{n_0}^* s_{n_1}^* s_{n_2} s_{n_3} \left[h_{n_1}^* h_{n_2} h_{n_3} \mathbf{f}_{n_0}^{(l)*} + \right. \\ & \left. h_{n_0}^* h_{n_2} h_{n_3} \mathbf{f}_{n_1}^{(l)*} + h_{n_0}^* h_{n_1}^* h_{n_3} \mathbf{f}_{n_2}^{(l)} + h_{n_0}^* h_{n_1}^* h_{n_2} \mathbf{f}_{n_3}^{(l)} \right]. \end{aligned} \quad (32)$$

For the sake of simplicity, let us denote $\mathcal{D}_{\mathcal{G}}$ as the set of indices in vector $\boldsymbol{\omega}$ that are zero due to the lack of connections between specific ports in the impedance network. By defining $\gamma \ll 1$ and setting

$$\tau^{(l)} = \gamma / \left\| (\mathbf{Z}^{(l)} + Z_0 \mathbf{I}_N)^{-1} \right\|_{\infty} \quad (33)$$

such that (28) holds, and leveraging Proposition 3 to remove the constraint in (26b), (26) can be transformed into a convex problem in the neighborhood of $\boldsymbol{\omega}^{(l)}$ as

$$\underset{\boldsymbol{\omega}}{\text{minimize}} \quad \xi_2 = -\mathbf{u}(\boldsymbol{\omega}^{(l)})^T \boldsymbol{\omega} \quad (34a)$$

$$\text{subject to} \quad \|\boldsymbol{\omega}\|_r \leq \tau^{(l)}, \forall r, \quad (34b)$$

$$[\boldsymbol{\omega}]_r = 0, r \in \mathcal{D}_{\mathcal{G}}, \quad (34c)$$

where (34c) ensures that $\boldsymbol{\Omega}$ has the same zero entries as \mathbf{Z} depending on the structure of BD-RIS. Note that for a fully-connected BD-RIS, constraint (34c) can be removed.

Theorem 2. *The local solution of (34) can be updated using*

$$\boldsymbol{\omega}^{(l+1)} = \boldsymbol{\omega}^{(l)} + \rho_{\omega} (\boldsymbol{\omega}^* - \boldsymbol{\omega}^{(l)}), \quad (35)$$

where $\rho_{\omega} \leq 1$ is a parameter utilized to control the convergence of the solution and

$$[\boldsymbol{\omega}^*]_r = \begin{cases} 0, & r \in \mathcal{D}_{\mathcal{G}}, \\ [\mathbf{u}^{(l)}]_r / 2\nu_r^{(l)}, & \text{otherwise}, \end{cases} \quad (36)$$

$$\nu_r^{(l)} = \begin{cases} 0, & r \in \mathcal{D}_{\mathcal{G}}, \\ \|\mathbf{u}^{(l)}\|_r / 2\tau^{(l)}, & \text{otherwise}. \end{cases} \quad (37)$$

Proof. The proof is provided in Appendix D.

We leverage Theorem 2 to solve (34) iteratively. Moreover, it was verified that $\text{Vec}(\boldsymbol{\Omega}^{(l+1)}) = \mathbf{P} \boldsymbol{\omega}^{(l+1)}$; thus, $\boldsymbol{\Omega}^{(l+1)} = \text{Vec}_{M,M}^{-1}(\text{Vec}(\boldsymbol{\Omega}^{(l+1)}))$ can be used for updating \mathbf{Z} as

$$\mathbf{Z}^{(l+1)} = \mathbf{Z}^{(l)} + j\Im\{\boldsymbol{\Omega}^{(l+1)}\}, \quad (38)$$

where only the imaginary part of $\boldsymbol{\Omega}^{(l+1)}$ is updated to ensure that the impedance matrix, i.e., \mathbf{Z} , remains imaginary.

Algorithm 4 illustrates the proposed iterative optimization method relying on alternating optimization, SCA, KKT conditions, and the Neumann approximation for BD-RIS-aided WPT (IT-BDRIS) given $\mathcal{D}_{\mathcal{G}}$. First, we initialize the variables such that the impedance matrix is set to reference impedance value, while (13) is used to initialize s_n . Then, the alternating optimization is done through lines 6-16. Specifically, each alternating optimization iteration consists of iteratively updating \mathbf{Z} given fixed $s_n, \forall n$ in lines 8-13, followed by obtaining $s_n, \forall n$ using Algorithm 1. This procedure is repeated iteratively until convergence.

Algorithm 4 Iterative beamforming and waveform optimization for BD-RIS-aided WPT relying on SCA, KKT, and the Neumann approximation (IT-BDRIS).

1: **Input:** $\mathcal{G}, \beta, v, \gamma, \mathbf{h}_{R,n}, \mathbf{h}_{I,n}, \forall n$ **Output:** $s_n^{(l)}, \forall n, \mathbf{Z}^{(l)}$
2: **Initialize:**
3: $f^* = 0, i_{dc} = \infty, [\mathbf{Z}^{(l)}]_{i,m} = jZ_0, \forall i, m$
4: Compute \mathbf{P}, h_n , and $\tau^{(l)}$ using (16), (30), and (33)
5: Initialize $s_n^{(l)}, \forall n$ using (13)
6: **repeat**
7: $\xi_2 = \infty, i_{dc}^* \leftarrow i_{dc}$
8: **repeat**
9: $\xi_2^* \leftarrow \xi_2$, compute $\nu_r^{(l)}, \forall r$ using (37)
10: Obtain $\mathbf{Z}^{(l+1)}$ using (36), (35), and (38)
11: Compute ξ_2 and $\tau^{(l+1)}$ using (34a) and (33)
12: $\mathbf{Z}^{(l)} \leftarrow \mathbf{Z}^{(l+1)}, \tau^{(l)} \leftarrow \tau^{(l+1)}, l \leftarrow l + 1$
13: **until** $\|1 - \xi_2^*/\xi_2\| \leq v$
14: Compute h_n using (30)
15: Run Algorithm 1 to update $s_n^{(l)}$, compute i_{dc} using (4)
16: **until** $\|1 - i_{dc}^*/i_{dc}\| \leq v$

D. Complexity Analysis

Herein, we discuss the time complexity of the proposed algorithms in details:

IT-WF: The time complexity at each optimization iteration is $\mathcal{O}(N)$, which corresponds to the computation of s_n .

SDR-BDRIS: The number of variables in (25) is $\bar{M}(\bar{M} + 1)/2$ with $\bar{M} = M(M + 1)/2$, while the rest of the entries in \mathbf{X} are determined according to the Hermitian structure, and the size of these Hermitian matrix sub-space is \bar{M}^2 . Additionally, the number of constraints scales with M in (25). For a given accuracy, the complexity of SDP grows at most with $\mathcal{O}(n^{1/2})$, where n is the problem size, determined by the number of constraints and variables [45]. Thus, the SDR-BDRIS converges in polynomial time and its complexity increases with K and \bar{M}^2 combined with complexity for IT-WF. Thus, it is evident that the complexity of SDR-BDRIS is significantly higher than IT-BDRIS since \bar{M}^2 can become difficult to handle for large BD-RIS size.

IT-BDRIS: In the most time-consuming case, i.e., fully connected impedance network, $\boldsymbol{\omega}$ includes \bar{M} non-zero entries, leading to $\mathcal{O}(\bar{M})$ complexity for obtaining the solution and the dual variables. Combining this with the negligible complexity for obtaining $\mathbf{Z}^{(l+1)}$ leads to $\mathcal{O}(\bar{M})$ time complexity for each optimization iteration. Combining this with the complexity of IT-WF evinces that the proposed IT-BDRIS is much more efficient than the traditional solver-based SCA.

IV. NUMERICAL ANALYSIS

In this section, we evaluate the system's performance in a WiFi-like scenario with $f_c = 2.4$ GHz, a bandwidth of $\text{BW} = 10$ MHz, and $\Delta f = \text{BW}/N$. We consider the path loss due to large-scale fading at a distance d to be $L_0 d^{-\kappa}$, where $L_0 = 40$ dB is the reference path loss at 1 m distance and $\kappa = 2$ is the exponent. Moreover, the incident and reflected paths are both considered to be 2 m. Finally, the rectifier parameters

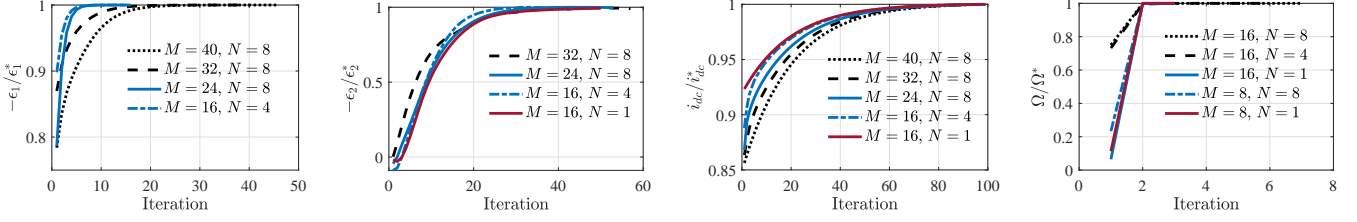


Fig. 2: The convergence performance of (a) IT-WF (left), (b) iterative beamforming (middle-left), (c) IT-BDRIS for joint optimization (middle-right), (d) SDR-BDRIS for joint optimization (right). We adopt a random channel realization and assume a fully-connected BD-RIS and several M and N combinations.

are selected based on the circuit simulations in [8], [22] for small-signal regime such that $K_2 = 0.17$ and $K_4 = 957.25$.

Channels are modeled with quasi-static Rician fading as

$$\mathbf{h}_n = \sqrt{\kappa/(\kappa+1)}\mathbf{h}_n^{\text{LoS}} + \sqrt{1/(\kappa+1)}\mathbf{h}_n^{\text{NLoS}}, \quad (39)$$

where κ is the Rician factor and the $\mathbf{h}_n^{\text{LoS}}$ is modeled using the far-field LoS channel for uniform planar arrays. The NLoS part is modeled with Rayleigh fading considering $L = 18$ delay taps with realizations following a circularly symmetric complex Gaussian distribution with a random power p_l , such that $\sum_{l=1}^L p_l = 1$. Furthermore, we introduce an additional parameter α for the NLoS part such that the coherence bandwidth is $B_c = \alpha \text{BW}$. Hereby, the delay spread is $\varsigma = 1/B_c$, while the maximum delay spread is considered to be $\varsigma_m = 2\varsigma$. Then, the tap delays $t_l, \forall l$ are generated uniformly spaced up to ς_m , and the frequency response of each tap at the n th sub-carrier is multiplied by its corresponding delay term $e^{j2\pi f_n t_l}$. Hereby, selecting a small α such that B_c is much smaller than BW leads to more frequency selectivity of the channel. Nevertheless, a large α leads to $B_c \gg \text{BW}$, which means all delay taps can be received within the coherence bandwidth, leading to a frequency-flat channel. The results are averaged over 200 random channel realizations unless otherwise stated.

A. Convergence Analysis

Fig. 2 illustrates the convergence performance of the IT-BDRIS, IT-WF, iterative passive beamforming, and SDR-BDRIS. As seen in Fig. 2.a and Fig. 2.b, both beamforming and waveform optimization algorithms iteratively converge toward a local optimum solution. Moreover, the number of required iterations increases with M and N as discussed in Section III-D. Moreover, Fig. 2.c and Fig. 2.d highlight that the proposed methods for alternating optimization of waveform and passive beamforming lead to convergence. Although the number of iterations in SDR-BDRIS is lower than in IT-BDRIS, each iteration of SDR-BDRIS requires solving multiple SDP problems with high complexity. At the same time, IT-BDRIS relies only on closed-form computations. Observe that the number of iterations for different setups is the same in SDR-BDRIS, but the time complexity of solving (25) drastically increases with M since the hermitian matrix subspace scales with M^4 .

B. Algorithms Performance Comparison

Herein, we compare the performance of the proposed algorithms and consider also an optimal benchmark derived for

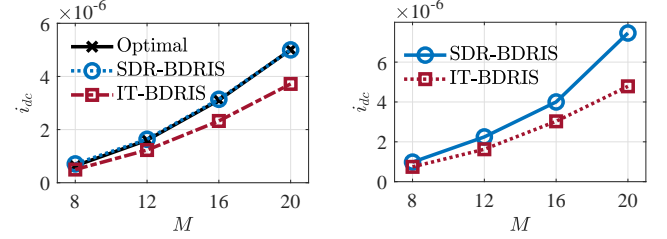


Fig. 3: Average i_{dc} at the ER as a function of M using different algorithms for (a) $N = 1$ (left) and (b) $N = 4$ (right) with NLoS channel ($\alpha = 0.1$), $P_T = 50$ dBm, and a fully-connected BD-RIS.

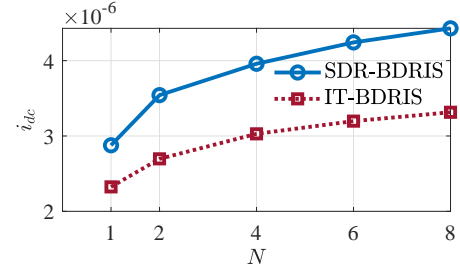


Fig. 4: Average i_{dc} at the ER as a function of N using different algorithms with $\alpha = 0.1$, $M = 16$ and $P_T = 50$ dBm, and a fully-connected BD-RIS .

$N = 1$. Note that for a single-carrier system ($N = 1$), problem (5) becomes equivalent to maximizing the RF power, i.e., the second-order term in i_{dc} , in terms of the solution. Thus, the framework introduced in [36] serves as a benchmark when $N = 1$ and is labeled as optimal in Fig. 3.a.

Fig. 3 compares the performance of the proposed algorithms for $N = 1$ and $N = 4$ as a function of M . Note that SDR-BDRIS achieves optimal performance, while IT-BDRIS leads to relatively lower i_{dc} values, but is still close to the optimal solution and the gap increases with M . Moreover, for $N = 4$, the same trend is observed, where SDR-BDRIS outperforms IT-BDRIS. However, as stated earlier, the complexity of SDR-BDRIS is considerably higher than that of IT-BDRIS, especially for large M ; thus, a trade-off exists between performance and complexity. Note that there is no optimal benchmark for the multi-carrier case. Fig. 4 compares the performance of the proposed algorithms as a function of N , where SDR-BDRIS outperforms IT-BDRIS also in this case.

Table I: SDP-BDRIS and SDR-BDRIS performance comparison with 5 random realizations of Rayleigh fading channel.

Setup	SDP-BDRIS		SDR-BDRIS	
	$i_{dc} (\mu A)$	DR	$i_{dc} (\mu A)$	DR
$M = 4, N = 8$	0.25	0.995	0.25	0.573
$M = 8, N = 4$	1.04	0.998	1.04	0.57
$M = 8, N = 8$	1.25	0.997	1.25	0.551
$M = 12, N = 8$	2.08	0.996	2.08	0.684

Table I compares the SDR-BDRIS and the method that models the rank-1 constraint using (21), which is referred to as SDP-BDRIS.⁶ Herein, we illustrate the eigenvalue dominance ratio (DR) for each algorithm, which is computed by dividing the dominant eigenvalue of the obtained \mathbf{X} by the sum of eigenvalues. It can be seen that the DR of SDP-BDRIS is much higher than SDR-BDRIS, ensuring a rank-1 solution. On the other hand, the DR values of SDR-BDRIS verify that it does not guarantee a rank-1 solution, and leveraging approximations to obtain a feasible solution is inevitable. Interestingly, it is observed that both algorithms lead to similar i_{dc} , and the rank-1 approximations of SDR-BDRIS only reduce its complexity and do not lead to performance losses.

C. Waveform Behaviour & Channel Analysis

One of the key considerations of WPT with non-linear EH is the operating regime of the rectifier. Specifically, if the input RF power to the rectifier is relatively low, the RF-to-DC conversion efficiency drops significantly. On the other hand, if the RF input power is high such that the rectifier's diode enters the breakdown region, the mathematical model for the small-signal regime is no longer valid. Thus, it is important to select P_T properly such that the received RF power is in the proper regime [8]. For this, we proceed with some discussions on the system's behavior for different P_T values.

Fig. 5 presents the normalized gain of the channels and input signal for different P_T and α values. Interestingly, we can see that the variation among the gains of the cascade channel at different sub-carriers becomes smaller as the incident and reflective channels become less frequency-selective (increasing α), but obviously P_T has no impact on it. This is caused by the nature of frequency-flat channels, where the channel values at different sub-carriers are almost equal, leading to the BD-RIS configuration impacting them similarly. However, when the channel becomes more frequency-selective, the BD-RIS configuration impacts the independent channels at different sub-carriers differently. Moreover, the power allocation pattern among the different sub-carriers of the input signal also changes with both P_T and α . Indeed, for low P_T , the whole power budget tends to be allocated to one or a few sub-carriers, especially as α decreases. The reason is that when P_T is relatively small such that the input RF power to the rectifier is low, the rectifier operates in the low-efficiency regime. This leads to the fourth-order term of DC power being negligible and the second-order term

becoming dominant. Thus, the designed waveform does not leverage all sub-carriers efficiently to generate a high peak-to-average power ratio (PAPR). On the other hand, when P_T is chosen such that the RF power is in the desired range ($P_T = 50$ dBm in this case), the rectifier operates in the high-efficiency regime, and the fourth-order term becomes large enough to impact the DC harvested power leading to a more diverse pattern in power allocation among sub-carriers. Thus, P_T needs to match properly with system parameters so that the rectifier non-linearity is leveraged efficiently. For instance, when $P_T = 50$ dBm, the power is allocated to the stronger sub-carriers in a frequency-selective scenario, while the power is allocated to all sub-carriers in a frequency-flat case with $\alpha = 10$. Motivated by this analysis, we consider $P_T = 50$ dBm in the rest of this section.

Fig. 6 shows the time domain signal for the same channel realizations as in Fig. 5. Note that higher PAPR signals are received at the ER for $P_T = 50$ dBm to leverage the rectifier's non-linearity efficiently, even for lower α . On the other hand, for low P_T , the received signal has PAPR ≈ 0 dB for small α and lower PAPR compared to $P_T = 50$ dBm for large values of α . Thus, as earlier stated, high PAPR signals are beneficial to leverage the rectifier's non-linearity, but only when the input RF power is in the high-efficiency regime of the rectifier.

D. D-RIS versus BD-RIS

Herein, we compare the performance of D-RIS and fully connected BD-RIS. The BD-RIS results are obtained using the SDR-BDRIS approach, while for D-RIS, this approach can be straightforwardly modified as presented in [34].

Note that for far-field LoS, the channel is deterministic and is computed using the relative phase difference of elements. Thus, we assume that the variation among the sub-carriers is negligible such that for a given Θ , $h_n = h$. Hereby, (4) can be rewritten as $\alpha_1 \|h\|^2 + \alpha_2 \|h\|^4$, where α_1 and α_2 are positive coefficients depending on the waveform and rectenna circuit. To maximize this, it is sufficient to maximize the cascade channel gain $\|h\|$, which can be achieved by constructing a diagonal Θ such that $[\Theta]_{i,i} = e^{-j([\tilde{\mathbf{h}}_{R,n}]_i + [\tilde{\mathbf{h}}_{T,n}]_i)}$, $\forall i$. Such a scattering matrix can be designed using D-RIS; thus, D-RIS can achieve the optimal performance and BD-RIS does not introduce any additional gain. Moreover, for $N = 1$, (5) becomes equivalent to maximizing the RF power, which allows for extending the findings of [16] to single-carrier WPT. Thus, for a channel with NLoS components, we expect that BD-RIS outperforms D-RIS even with a continuous wave.

Fig. 7 illustrates the average i_{dc} as a function of M for D-RIS and BD-RIS. It is seen in Fig. 7.a that for far-field LoS channels, BD-RIS achieves the same performance as D-RIS in both single-carrier and multi-carrier systems, which complies with the mathematical analysis. However, when the channel tends to become frequency-selective, as in Fig. 7.b, BD-RIS can leverage the extra degrees of freedom to impact different channel components effectively such that i_{dc} becomes higher compared to D-RIS. Fig. 8 verifies the same pattern over N with a given M . Specifically, BD-RIS and D-RIS achieve the same performance for any N under LoS, while for the Rician

⁶Due to the high complexity of SDP-BDRIS, extensive simulations result in significant time overhead. Therefore, a brief comparison is presented to highlight the relative differences in the outcomes.

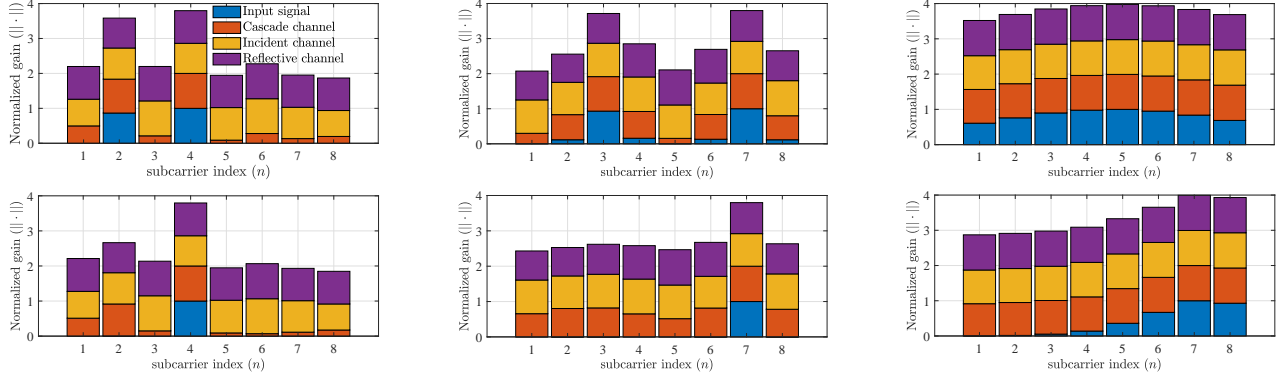


Fig. 5: The normalized gain of the channels and input signal at different sub-carriers for (a) $P_T = 50$ dBm (top) and (b) $P_T = 30$ dBm (bottom) for $\alpha = 0.1$ (left), $\alpha = 1$ (middle), and $\alpha = 10$ (right). We assume a fully-connected BD-RIS with $M = 32$, $N = 8$, and a pure NLoS ($\kappa = 0$) random channel realization. Note that the bars are represented in a stacked fashion, meaning that bars with the same length represent the same normalized gain.

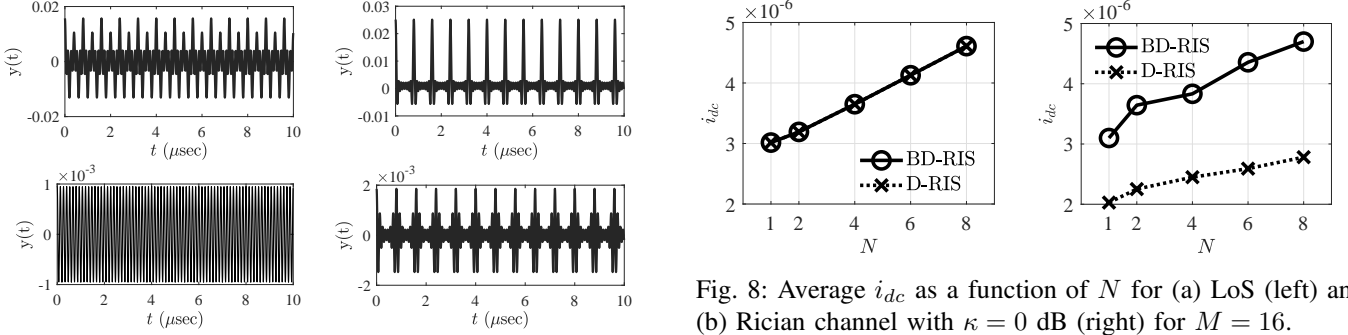


Fig. 6: The received signal in time domain for (a) $P_T = 50$ dBm (top) and (b) $P_T = 30$ dBm (bottom) for $\alpha = 1$ (left) and $\alpha = 10$ (right) with fully-connected BD-RIS, $M = 32$, and $N = 8$ at a random channel realization.

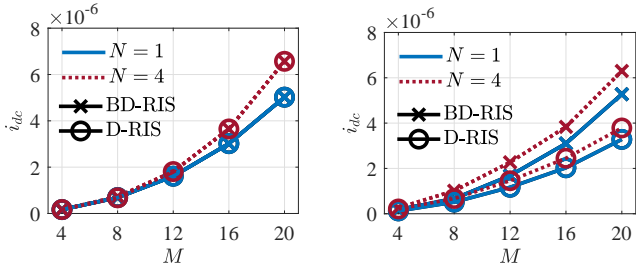


Fig. 7: Average i_{dc} as a function of M for (a) LoS (left) and (b) Rician channel with $\kappa = 0$ dB (right).

channel with NLoS components, the BD-RIS outperforms D-RIS and the performance gap increases with N .

Fig. 9 illustrates the normalized gain of the channels and the input signal at different sub-carriers. It is observed that the configuration of D-RIS/BD-RIS impacts the sub-carriers similarly under pure LoS, leading to small variations in the cascade channel. Thus, D-RIS provides sufficient degrees of freedom to compensate for the channels. On the other hand, for NLoS, BD-RIS leverages its additional degrees of freedom to create more dominant sub-carriers compared to D-RIS, leading

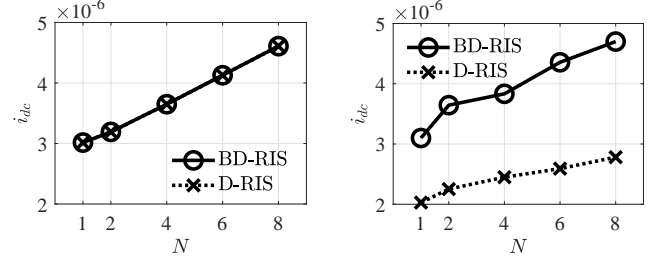


Fig. 8: Average i_{dc} as a function of N for (a) LoS (left) and (b) Rician channel with $\kappa = 0$ dB (right) for $M = 16$.

to extra performance gains for frequency-selective channels.

V. CONCLUSION

We considered a BD-RIS-aided SISO WPT system with EH non-linearity. Moreover, we formulated a joint beamforming and waveform optimization problem aiming to maximize the harvested power at the ER. To address this problem, we decoupled the waveform optimization and beamforming problems and leveraged alternating optimization. We proposed an efficient iterative method for waveform optimization and three beamforming approaches namely SDR-BDRIS, SDP-BDRIS, and IT-BDRIS. Furthermore, IT-BDRIS has the lowest computational complexity but in cost of performance losses. Meanwhile, It was seen that SDR-BDRIS achieves the same performance as SDP-BDRIS with less computational complexity. The simulation results proved that the proposed algorithms converge to a local optimal solution, while the complexity scales with the number of RIS elements and the number of sub-carriers. Moreover, SDR-BDRIS achieves the optimal performance for a single-carrier system and outperforms IT-BDRIS in other scenarios. Interestingly, we proved that BD-RIS achieves the same performance as D-RIS under LoS conditions (in the absence of mutual coupling), while it outperforms D-RIS in NLoS cases. Furthermore, our findings demonstrated that the frequency selectivity of the channel impacts the way that BD-RIS shapes the cascade channel.

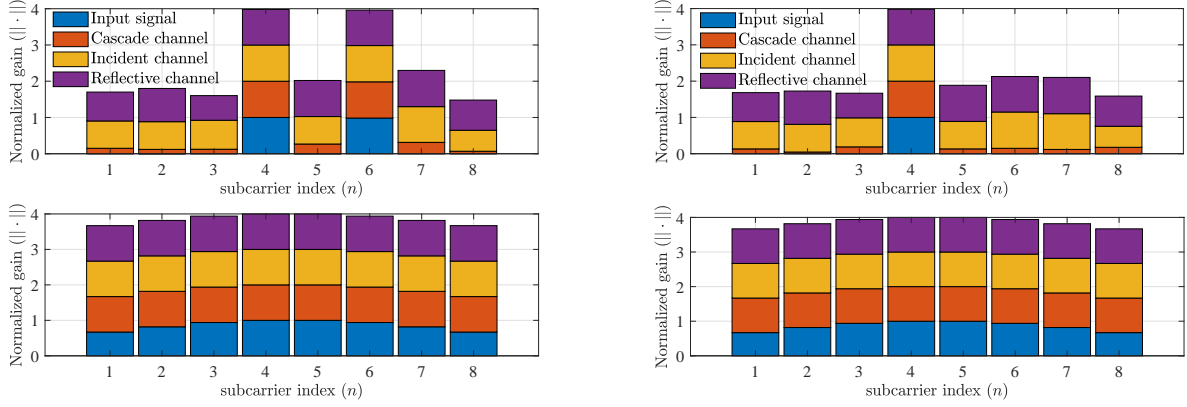


Fig. 9: The normalized gain of the channels and input signal at different sub-carriers for (a) NLoS channel (top) and (b) LoS channel (bottom) for BD-RIS (left) and D-RIS (right). We assume a random channel realization with $M = 16$.

Finally, we showed that the waveform power allocation to different sub-carriers depends on the transmit power and the rectifier's operating regime.

APPENDIX A PROOF OF THEOREM 1

Let us proceed by writing the Lagrangian of (6) as

$$\mathcal{L}(\bar{s}_n) = - \sum_{n=1}^N g(\bar{s}_n^{(l)}) \bar{s}_n + \lambda^{(l)} \left(\frac{1}{2} \sum_{n=1}^N \bar{s}_n^2 - P_T \right), \quad (40)$$

where $\lambda^{(l)}$ is the dual variable corresponding to (9b). Then, we can write the derivative of (40) w.r.t. \bar{s}_n as

$$\frac{\partial \mathcal{L}(\bar{s}_n)}{\partial \bar{s}_n} = -g(\bar{s}_n^{(l)}) + \lambda^{(l)} \bar{s}_n, \quad \forall n. \quad (41)$$

By setting (41) to zero, we attain (11). Moreover, the optimal solution must utilize the whole transmit power budget, i.e., $\frac{1}{2} \sum_{n=1}^N \bar{s}_n^2 = P_T$. Thus, by substituting (11) into the latter equality, the dual variable $\lambda^{(l)}$ is given by (12). Finally, we introduce an additional parameter $\rho_s \leq 1$ to control the convergence of the solution such that the subgradient update is given by (10). \square

APPENDIX B PROOF OF PROPOSITION 1

We proceed by rewriting h_n as

$$\begin{aligned} h_n &= \mathbf{h}_{R,n}^T \mathbf{\Theta} \mathbf{h}_{I,n} = \text{Tr}(\mathbf{h}_{R,n}^T \mathbf{\Theta} \mathbf{h}_{I,n}) \\ &\stackrel{(a)}{=} \text{Tr}(\mathbf{h}_{I,n} \mathbf{h}_{R,n}^T \mathbf{\Theta}) = \text{Tr}(\mathbf{H}_n \mathbf{\Theta}) \\ &\stackrel{(b)}{=} \text{Vec}(\mathbf{H}_n)^T \text{Vec}(\mathbf{\Theta}) \stackrel{(c)}{=} \text{Vec}(\mathbf{H}_n)^T \mathbf{P} \boldsymbol{\theta} = \mathbf{a}_n^T \boldsymbol{\theta}. \end{aligned} \quad (42)$$

Assume that \mathbf{D} , \mathbf{F} , and \mathbf{H} are arbitrary matrices. Hereby, (a) and (b) come from $\text{Tr}(\mathbf{D}\mathbf{F}\mathbf{H}) = \text{Tr}(\mathbf{H}\mathbf{D}\mathbf{F})$ and $\text{Tr}(\mathbf{D}^T \mathbf{F}) = \text{Vec}(\mathbf{D})^T \text{Vec}(\mathbf{F})$, respectively. Moreover, by defining $\boldsymbol{\theta} \in \mathbb{C}^{\bar{M} \times 1}$ as the vector containing the lower/upper-triangle elements in $\mathbf{\Theta}$, one can design a permutation matrix $\mathbf{P} \in \{0, 1\}^{M^2 \times \bar{M}}$ such that $\mathbf{P}\boldsymbol{\theta} = \text{Vec}(\mathbf{\Theta})$ holds, which leads to (c). \square

APPENDIX C PROOF OF PROPOSITION 2

The Neumann approximation can be used to approximate the inverse of a matrix using another close matrix. Imagine \mathbf{A} is a close matrix to an invertible \mathbf{X} , such that [46]

$$\lim_{n \rightarrow \infty} (\mathbf{I} - \mathbf{A}\mathbf{X}^{-1})^n = 0. \quad (43)$$

Then, the inverse of \mathbf{A} can be written using the Neumann series as [47]

$$\mathbf{A}^{-1} \approx \sum_{i=0}^{\infty} (\mathbf{X}^{-1}(\mathbf{X} - \mathbf{A}))^i \mathbf{X}^{-1}. \quad (44)$$

Now, let us consider $\boldsymbol{\Omega}$ as a small increment to the impedance matrix \mathbf{Z} , such that $\|[\boldsymbol{\Omega}]_{i,m}\| \leq \delta, \forall i, m$, leading to $\mathbf{Z} + \boldsymbol{\Omega}$ being close to \mathbf{Z} . Hereby, we can write the first-order Neumann series as in (27). Note that the first-order approximation might lead to losing some information about higher-order terms. However, it has been proven that (27) is sufficiently accurate if δ satisfies (28) [37], [47], [48], leading to the error of the approximation approaching zero. \square

APPENDIX D PROOF OF THEOREM 2

We proceed by defining $\bar{M} = M(M+1)/2$ and writing the Lagrangian of (34) as

$$\begin{aligned} \mathcal{L}(\boldsymbol{\omega}) &= - \sum_{r=1}^{\bar{M}} [\mathbf{u}^{(l)}]_r [\boldsymbol{\omega}]_r \\ &\quad + \sum_{r=1}^{\bar{M}} \nu_r^{(l)} \left(\|\boldsymbol{\omega}\|_r^2 - \tau^{(l)2} \right) + \sum_{r \in \mathcal{D}_g} \bar{\lambda}_r^{(l)} [\boldsymbol{\omega}]_r. \end{aligned} \quad (45)$$

It is obvious that by forcing $[\boldsymbol{\omega}]_r = 0, \forall r \in \mathcal{D}_g$, we have $\bar{\lambda}_r^{(l)} [\boldsymbol{\omega}]_r = 0, \forall r \in \mathcal{D}_g$. Meanwhile, for $r \notin \mathcal{D}_g$, the derivative of the Lagrangian function is given by

$$\frac{\partial \mathcal{L}(\boldsymbol{\omega})}{\partial [\boldsymbol{\omega}]_r} = -[\mathbf{u}^{(l)}]_r + 2\nu_r^{(l)} [\boldsymbol{\omega}]_r, \quad r \notin \mathcal{D}_g. \quad (46)$$

We know that the solution must satisfy KKT conditions [42]. Hence, by setting the derivative to zero we can write the

closed-form expression of the solution at the l th iteration as in (36). Then, using the complementary slackness for the dual variable $\nu_r^{(l)}$, and leveraging (36) and the fact that $\nu_r^{(l)} \geq 0, \forall r$, we have (37). Similar to Theorem 1, we introduce $\rho_\omega \leq 1$ to control the convergence of the solution, leading to (35) giving the solution at the end of the l th iteration. \square

REFERENCES

- [1] Z. Zhang *et al.*, “6G wireless networks: vision, requirements, architecture, and key technologies,” *IEEE Veh. Technol. Mag.*, vol. 14, no. 3, pp. 28–41, 2019.
- [2] N. H. Mahmood *et al.*, “Six key features of machine type communication in 6G,” in *2nd 6G SUMMIT*, pp. 1–5, 2020.
- [3] O. Lopez *et al.*, “High-Power and Safe RF Wireless Charging: Cautious Deployment and Operation,” *IEEE Wireless Commun.*, pp. 1–8, 2024.
- [4] 3GPP, “Study on Ambient IoT (Internet of Things) in RAN,” Tech. Rep. 38.848, 2023.
- [5] O. López *et al.*, “Zero-energy Devices for 6G: Technical Enablers at a Glance,” 2024.
- [6] O. López *et al.*, “Massive wireless energy transfer: enabling sustainable IoT toward 6G era,” *IEEE Internet Things J.*, vol. 8, no. 11, pp. 8816–8835, 2021.
- [7] B. Clerckx *et al.*, “Waveform optimization for wireless power transfer with nonlinear energy harvester modeling,” in *ISWCS*, pp. 276–280, 2015.
- [8] B. Clerckx and J. Kim, “On the beneficial roles of fading and transmit diversity in wireless power transfer with nonlinear energy harvesting,” *IEEE Trans. Wirel. Commun.*, vol. 17, no. 11, pp. 7731–7743, 2018.
- [9] I. Ahmed *et al.*, “A Survey on Hybrid Beamforming Techniques in 5G: Architecture and System Model Perspectives,” *IEEE Commun. Surv. Tutor.*, vol. 20, no. 4, pp. 3060–3097, 2018.
- [10] H. Zhang *et al.*, “Near-field wireless power transfer with dynamic metasurface antennas,” in *IEEE SPAWC*, pp. 1–5, 2022.
- [11] A. Azarbahram *et al.*, “Energy Beamforming for RF Wireless Power Transfer With Dynamic Metasurface Antennas,” *IEEE Wireless Commun. Lett.*, vol. 13, no. 3, pp. 781–785, 2024.
- [12] Q. Wu *et al.*, “Intelligent Reflecting Surface-Aided Wireless Communications: A Tutorial,” *IEEE Trans Commun.*, vol. 69, no. 5, pp. 3313–3351, 2021.
- [13] R. Long *et al.*, “Active Reconfigurable Intelligent Surface-Aided Wireless Communications,” *IEEE Trans. on Wireless Commun.*, vol. 20, no. 8, pp. 4962–4975, 2021.
- [14] S. Zhang *et al.*, “Intelligent omni-surfaces: Ubiquitous wireless transmission by reflective-refractive metasurfaces,” *IEEE Trans. on Wireless Commun.*, vol. 21, no. 1, pp. 219–233, 2022.
- [15] H. Li *et al.*, “Reconfigurable Intelligent Surfaces 2.0: Beyond Diagonal Phase Shift Matrices,” *IEEE Commun. Mag.*, vol. 62, no. 3, pp. 102–108, 2024.
- [16] S. Shen *et al.*, “Modeling and Architecture Design of Reconfigurable Intelligent Surfaces Using Scattering Parameter Network Analysis,” *IEEE Trans. on Wireless Commun.*, vol. 21, no. 2, pp. 1229–1243, 2022.
- [17] M. Nerini *et al.*, “Closed-Form Global Optimization of Beyond Diagonal Reconfigurable Intelligent Surfaces,” *IEEE Trans. Wirel. Commun.*, vol. 23, no. 2, pp. 1037–1051, 2024.
- [18] M. Nerini and B. Clerckx, “Pareto Frontier for the Performance-Complexity Trade-Off in Beyond Diagonal Reconfigurable Intelligent Surfaces,” *IEEE Commun. Lett.*, vol. 27, no. 10, pp. 2842–2846, 2023.
- [19] H. Li, S. Shen, and B. Clerckx, “Beyond diagonal reconfigurable intelligent surfaces: A multi-sector mode enabling highly directional full-space wireless coverage,” *IEEE JSAC*, vol. 41, no. 8, pp. 2446–2460, 2023.
- [20] H. Li, S. Shen, and B. Clerckx, “Beyond diagonal reconfigurable intelligent surfaces: From transmitting and reflecting modes to single-, group-, and fully-connected architectures,” *IEEE Trans. on Wireless Commun.*, vol. 22, no. 4, pp. 2311–2324, 2023.
- [21] S. Shen and B. Clerckx, “Beamforming Optimization for MIMO Wireless Power Transfer With Nonlinear Energy Harvesting: RF Combining Versus DC Combining,” *IEEE Trans. Wirel. Commun.*, vol. 20, no. 1, pp. 199–213, 2021.
- [22] B. Clerckx and E. Bayguzina, “Waveform Design for Wireless Power Transfer,” *IEEE Trans. Signal Process.*, vol. 64, no. 23, pp. 6313–6328, 2016.
- [23] B. Clerckx and E. Bayguzina, “Low-Complexity Adaptive Multisine Waveform Design for Wireless Power Transfer,” *IEEE Antennas Wirel. Propag. Lett.*, vol. 16, pp. 2207–2210, 2017.
- [24] A. Azarbahram *et al.*, “Deep Reinforcement Learning for Multi-User RF Charging with Non-linear Energy Harvesters,” *IEEE Globecom* 2024.
- [25] Y. Huang and B. Clerckx, “Large-Scale Multiantenna Multisine Wireless Power Transfer,” *IEEE Trans. Signal Process.*, vol. 65, no. 21, pp. 5812–5827, 2017.
- [26] S. Shen and B. Clerckx, “Joint Waveform and Beamforming Optimization for MIMO Wireless Power Transfer,” *IEEE Trans Commun.*, vol. 69, no. 8, pp. 5441–5455, 2021.
- [27] Y. Zhang and B. Clerckx, “Waveform Design for Wireless Power Transfer With Power Amplifier and Energy Harvester Non-Linearities,” *IEEE Trans. Signal Process.*, pp. 1–15, 2023.
- [28] O. López *et al.*, “Massive MIMO with radio stripes for indoor wireless energy transfer,” *IEEE Trans. Wirel. Commun.*, vol. 21, no. 9, pp. 7088–7104, 2022.
- [29] O. López *et al.*, “A Low-Complexity Beamforming Design for Multiuser Wireless Energy Transfer,” *IEEE Wireless Commun. Lett.*, vol. 10, no. 1, pp. 58–62, 2021.
- [30] A. Azarbahram *et al.*, “On the Radio Stripe Deployment for Indoor RF Wireless Power Transfer,” in *IEEE WCNC*, pp. 1–6, 2024.
- [31] A. Azarbahram, O. López, and M. Latva-Aho, “Waveform Optimization and Beam Focusing for Near-field Wireless Power Transfer with Dynamic Metasurface Antennas and Non-linear Energy Harvesters,” *IEEE Trans. Wirel. Commun.*, pp. 1–1, 2024.
- [32] O. T. Demir and T. E. Tuncer, “Antenna Selection and Hybrid Beamforming for Simultaneous Wireless Information and Power Transfer in Multi-Group Multicasting Systems,” *IEEE Trans. on Wireless Commun.*, vol. 15, no. 10, pp. 6948–6962, 2016.
- [33] Y. Cheng, W. Peng, and T. Jiang, “Self-Sustainable RIS Aided Wireless Power Transfer Scheme,” *IEEE Trans. Veh. Technol.*, vol. 72, no. 1, pp. 881–892, 2023.
- [34] Z. Feng *et al.*, “Waveform and Beamforming Design for Intelligent Reflecting Surface Aided Wireless Power Transfer: Single-User and Multi-User Solutions,” *IEEE Trans. Wirel. Commun.*, vol. 21, no. 7, pp. 5346–5361, 2022.
- [35] Y. Zhao *et al.*, B. Clerckx, and Z. Feng, “IRS-Aided SWIPT: Joint Waveform, Active and Passive Beamforming Design Under Nonlinear Harvester Model,” *IEEE Trans. on Commun.*, vol. 70, no. 2, pp. 1345–1359, 2022.
- [36] M. Nerini *et al.*, “Beyond diagonal reconfigurable intelligent surfaces utilizing graph theory: Modeling, architecture design, and optimization,” *IEEE Trans. Wirel. Commun.*, pp. 1–1, 2024.
- [37] H. Li *et al.*, “Beyond Diagonal Reconfigurable Intelligent Surfaces With Mutual Coupling: Modeling and Optimization,” *IEEE Commun. Lett.*, vol. 28, no. 4, pp. 937–941, 2024.
- [38] A. Azarbahram *et al.*, “Beyond Diagonal Reconfigurable Intelligent Surfaces for Multi-Carrier RF Wireless Power Transfer,” 2025.
- [39] M. W. Shabir *et al.*, “Electromagnetically consistent optimization algorithms for the global design of ris,” *IEEE Wirel. Commun. Lett.*, pp. 1–1, 2025.
- [40] M. Nerini *et al.*, “A universal framework for multiport network analysis of reconfigurable intelligent surfaces,” *IEEE Trans. on Wireless Commun.*, pp. 1–1, 2024.
- [41] A. Abrardo, A. Toccafondi, and M. Di Renzo, “Design of reconfigurable intelligent surfaces by using s-parameter multiport network theory—optimization and full-wave validation,” *IEEE Trans. on Wireless Commun.*, vol. 23, no. 11, pp. 17084–17102, 2024.
- [42] S. Boyd and L. Vandenberghe, *Convex optimization*. Cambridge university press, 2004.
- [43] M. Grant and S. Boyd, “CVX: Matlab software for disciplined convex programming, version 2.1,” <http://cvxr.com/cvx>, Mar. 2014.
- [44] W.-K. Ma, P.-C. Ching, and Z. Ding, “Semidefinite relaxation based multiuser detection for M-ary PSK multiuser systems,” *IEEE Trans. Signal Process.*, vol. 52, no. 10, pp. 2862–2872, 2004.
- [45] L. Vandenberghe and S. Boyd, “Semidefinite Programming,” *SIAM Review*, vol. 38, no. 1, pp. 49–95, 1996.
- [46] M. Wu *et al.*, “Approximate matrix inversion for high-throughput data detection in the large-scale MIMO uplink,” in *IEEE ISCAS 2013*, pp. 2155–2158, 2013.
- [47] G. W. Stewart, *Matrix algorithms: volume 1: basic decompositions*. SIAM, 1998.
- [48] X. Qian and M. Di Renzo, “Mutual Coupling and Unit Cell Aware Optimization for Reconfigurable Intelligent Surfaces,” *IEEE Wirel. Commun. Lett.*, vol. 10, no. 6, pp. 1183–1187, 2021.